Exp Fluids (2008) 45:557–572
DOI 10.1007/s00348-008-0481-9

RESEARCH ARTICLE

On improvement of PIV image interrogation near stationary interfaces

R. Theunissen · F. Scarano · M. L. Riethmuller

Received: 15 November 2007 / Revised: 7 February 2008 / Accepted: 7 February 2008 / Published online: 9 March 2008

Abstract In this paper the problem posed by interfaces when present in PIV measurements is addressed. Different image pre-processing, processing and post-processing methodologies with the intention to minimize the interface effects are discussed and assessed using Monte Carlo simulations. Image treatment prior to the correlation process is shown to be incapable of fully removing the effects of the intensity pedestal across the object edge. The inherent assumption of periodicity in the signal causes the FFT-based correlation technique to perform the worst when the correlation window contains a signal truncation. Instead, an extended version of the masking technique introduced by Ronneberger et al. (Proceedings of the 9th international symposium on applications of laser techniques to fluid mechanics, Lisbon, 1998) is able to minimize the interface-correlation, resolving only the particle displacement peak. Once the displacement vector is obtained, the geometric center of the interrogation area is not the correct placement. Instead, the centre of mass position allows an unbiased representation of the wall flow (Usera et al. in Proceedings of the 12th international symposium on applications of laser techniques to fluid mechanics, Lisbon, 2004). The aforementioned concepts have been implemented in an adaptive interrogation methodology (Theunissen et al. in Meas Sci Technol 18:275–287, 2007) where additionally non-isotropic resolution and re-orientation of the correlation windows is applied near the interface, maximizing the wall-normal spatial resolution. The increase in resolution and robustness are demonstrated by application to a set of experimental images of a flat-plate, subsonic, turbulent boundary layer and a hypersonic flow over a double compression ramp.

R. Theunissen (✉) · M. L. Riethmuller
von Karman Institute for Fluid Dynamics,
Chaussée de Waterloo 72, 1640 Rhode-St-Genèse, Belgium
e-mail: theuniss@vki.ac.be

M. L. Riethmuller
e-mail: riethmuller@vki.ac.be

F. Scarano
Faculty of Aerospace Engineering-Aerodynamics,
Delft University of Technology, Kluyverweg 1, 2629 HS Delft,
The Netherlands
e-mail: f.scanaro@lr.tudelft.nl

List of symbols

*	cross-correlation operation
a.i.i.	adaptive interface interrogation; increased sampling and non-isotropic window rotation
AR	aspect ratio
conv.	conventional interrogation methodology
δ	boundary layer thickness
Δx, Δy	horizontal and vertical image correlation offset
Δt	image time separation
$d\xi$	wall-normal distance
DCC	direct cross-correlation
enh.	correlation enhancements; vector relocation and SME-DCC
ϕ	correlation coefficient
FFT	fast Fourier transform
FOV	field of view
(η,ξ)	interface-fitted coordinate system
I	intensity distribution
I_a, I_b	intensity distributions recorded at respectively time 't' and '$t + \Delta t$'
I^o	undisturbed image intensity distribution
κ, B	logarithmic-law constants

k_B	intensity scaling parameter for the background intensity
k_R	intensity scaling parameter for reflections
MA	moving average
ν	kinematic viscosity
PDF	probability density function
PIV	particle image velocimetry
θ	boundary layer momentum thickness
ρ	radius of curvature
S	step function
SF_{max}	user-defined maximum stretching factor
SME	symmetric mask exclusion
T	top hat function
U_∞	freestream velocity
u	wall-tangent velocity component
u'	fluctuating wall-tangent velocity component
u^+, y^+	inner-law variables
u_τ	wall-friction velocity
V	total velocity
WOR	wall overlap ratio
W_s	correlation window size
W_S^+	non-dimensional window size expressed in wall units
WU	wall unit, 1 WU = u_τ/ν
(x,y)	CCD coordinate system

1 Introduction

Nowadays, the majority of image processing algorithms involve a correlation operation between two images to extract the motion of detectable features. The problem of PIV measurements close to interfaces due to the presence of strong reflections and/or appearance of ghost particles is widely recognized (Stanislas et al. 2003). These reflections constitute detectable features (Shi and Tomasi 1994) and will create anomalies within the correlation-map, biasing the measured displacements towards zero and decreasing the reliability of the image analysis. Lindken and Merzkirch (2002) made use of fluorescent particles and shadowgraphy in an attempt to filter out these unwanted reflections. Depardon et al. (2005) on the other hand reduced the effect of optical disturbances by painting the complete test section and object with fluorescent paint. By placing the camera under the Brewster angle with the interface, Lin and Perlin (1998) were able to minimize the mirror-like behavior. Especially when dealing with curved interfaces or multiphase flows, a change in camera orientation is not always the simplest and most straightforward solution. In addition, surface treatments are not always possible. The truncation in signal density (i.e., seeding density) and velocity gradients imposed by the submerged object are known to cause an additional distortion in the correlation maps (Gui et al. 2003; Keane and Adrian 1990) leading to less accurate tracer displacement estimates. In these cases adjustment of the experimental setup will not avoid the degrading influence of the signal truncation. Consequently it is interesting to investigate the possibility to minimize the effects arising from interfaces in the image processing stage.

Current image analysis software samples the recordings at fixed locations within a Cartesian grid where the user selected parameters (correlation window size and overlap) are applied globally. As such, the processing parameters set are not optimal near interfaces. One therefore commonly resorts to PIV algorithm improvement or image enhancement prior to the correlation operation. The performance of several image pre-processing, image processing and data post-processing routines are assessed within this paper when the field of view involves a static interface using computer generated PIV images.

In case of an interface, the windows overlapping it are susceptible to a lack of tracer particle images making the estimate of the displacement less reliable (Keane and Adrian 1992). Ideally the interface is completely excluded from the correlation process while taking into account a sufficient number of tracers by careful positioning and orientation of the correlation windows. The second part of this paper therefore presents an extension of the adaptive PIV algorithm presented by Theunissen et al. (2007). To improve the robustness of the PIV technique, correlation windows are rotated parallel to the interface boundary. Considerable improvements in resolution are achieved by augmenting the sampling rate near the object interface, while applying a stretching factor proportional to the radius of curvature of the object's surface.

The applicability of the proposed techniques to enhance robustness and resolution in case of real experimental conditions is further proclaimed with the study of a subsonic turbulent boundary layer flow and hypersonic flow over a double compression ramp.

2 Problem statement

Performing PIV measurements near interfaces, the experimentalist is confronted with the appearance of non-uniform image properties in the wall-normal direction and reflections, which are usually more intense than the individual particle images. Under this circumstance the image interrogation by cross-correlation is strongly affected. The mathematical expression of the cross-correlation operation between the intensity distributions 'I_a' and 'I_b' is presented in Eq. 1 for clarity.

$$\phi(m,n)=\sum_{i,j=1}^{W_S}\frac{\left(I_a(i,j)-\overline{I_a}\right)\cdot\left(I_b(i+m,j+n)-\overline{I_b}(m,n)\right)}{\sqrt{\sum_{i,j=1}^{W_S}\left(I_a(i,j)-\overline{I_a}\right)^2\cdot\sum_{i,j=1}^{W_S}\left(I_b(i+m,j+n)-\overline{I_b}(m,n)\right)^2}} \quad (1)$$

Calculating 'ϕ' in the spatial domain through direct cross-correlation (DCC), requires mean intensities $\overline{I}_a$ and $\overline{I}_b$ to be computed in a different way. Whereas the former is determined only once before the correlation operation, the latter must be calculated each time a new pixel offset (m,n) between the two distributions is chosen. The use of Fourier transforms on the other hand neglects the spatial dependency of $\overline{I}_b$ sufficing a mean intensity value subtraction in the interrogation areas prior to the correlation operation. An example of the distortion in the correlation map due to the presence of a step in the intensity distribution across the interface is shown in Fig. 1. The interface is represented as delimiting the region where particle images are present from an ideally dark region. The location in the correlation map indicating the displacement of the tracer particles is highlighted by the white arrow. However, a wide region of high-intensity is present around the origin, decreasing the peak detectability. Approaching closer to the wall will ultimately lead to an erroneous measurement of the displacement, either biased towards the origin or even false peak detection.

In Particle Image Velocimetry the signal consists of tracer particles sampling the flow from which velocity information can be extracted. The interface region may either contain no particle images (typical for opaque-diffuse surface properties) or contain some particle images due to light reflection at the wall (e.g., metallic objects, glass, etc.). In the first case the light intensity may drop at the interface causing a step-like discontinuity. In the latter case the intensity level is kept approximately constant while differences in refraction index between fluid and interface give additionally rise to strong reflections. A further discontinuity in background noise can be encountered across the interface due to an absence of secondary particle intensity scattering.

In their simplest form this signal truncation and reflection across the interface may be modeled by a step 'S' and top hat function 'T' respectively. Figure 2 pictorially presents the decomposition of a PIV recording of intensity 'I', affected by the truncation and reflection, into a summation of the product between the undisturbed image 'I^{o}' and the step, and the scaled step and top hat functions. The mathematical expression is presented in Eq. 2. The first term models the signal truncation while the last terms represent respectively the truncation in background noise and presence of reflections. Scaling parameters 'k_{B}' and 'k_{R}' are introduced and can be time-dependent if reflections vary in intensity between recordings.

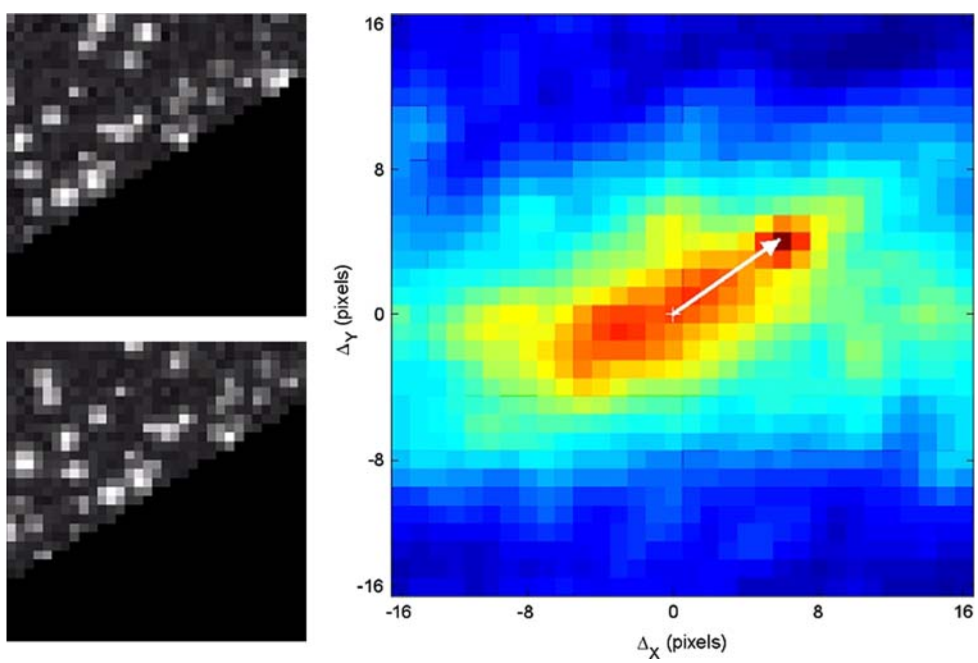

Fig. 1 Computer generated images with correlation map. White arrow indicates true imposed tracer displacement

$$I \approx (I^{\mathrm{o}} \cdot S) + k_{\mathrm{B}} \cdot S + k_{\mathrm{R}} \cdot T \tag{2}$$

According to Eq. 3 the cross-correlation of the signals 'I_{a}' and 'I_{b}' can be decomposed into the correlation of each term individually and cross-terms. The influence exerted by the step and top hat on the correlation map will therefore depend on the prominence of the truncation and will affect the entire correlation-map. For conciseness only the dominant terms in Eq. 3, being the autocorrelations and cross-correlation, are depicted in Fig. 2.

$$\begin{aligned} I_{\mathrm{a}} * I_{\mathrm{b}} \approx & \underbrace{\left(I_{\mathrm{a}}^{\mathrm{o}} \cdot S\right) * \left(I_{\mathrm{b}}^{\mathrm{o}} \cdot S\right)}_{\text{cross-correlation}} + \underbrace{k_{\mathrm{B}}^2 \cdot (S * S) + k_{\mathrm{R}}^2 \cdot (T * T)}_{\text{auto-correlations}} \\ & \underbrace{+ k_{\mathrm{B}} \cdot \left(\left(I_{\mathrm{a}}^{\mathrm{o}} + I_{\mathrm{b}}^{\mathrm{o}}\right) \cdot S\right) * S + k_{\mathrm{R}} \cdot \left(\left(I_{\mathrm{a}}^{\mathrm{o}} + I_{\mathrm{b}}^{\mathrm{o}}\right) \cdot S\right) * T + 2 \cdot k_{\mathrm{B}} k_{\mathrm{R}} \cdot (S * T)}_{\text{cross-terms}} \end{aligned} \tag{3}$$

From visual inspection the distortion in the measured signal's correlation can be traced back to the cross-correlation of the undisturbed images and the autocorrelation maps of the DC components ('S' and 'T'). These anomalies, which have maximum amplitudes at the origin, will undoubtedly cause a systematic error in the measured displacement, i.e., a bias towards zero, and in the worst case lead to spurious vectors due to poor signal peak detectability.

If coefficients 'k_{B}' and 'k_{R}' could be estimated as well as the interface location and extent, the influence exerted by the reflection and background truncation could be minimized, correcting the cross-correlation to

$$I_{\mathrm{a}} * I_{\mathrm{b}} \approx \left(I_{\mathrm{a}}^{\mathrm{o}} \cdot S\right) * \left(I_{\mathrm{b}}^{\mathrm{o}} \cdot S\right) \tag{4}$$

Possible means to estimate the coefficients are related to background intensity characterization (e.g., sliding mean filter, statistical minimum pixel intensity, etc.) while the interface can be detected through proper morphological operations (e.g., image erosion, edge detection, etc.). The signal truncation however cannot be removed by mere intensity-related transformations but must instead be dealt with by an adequate correlation method. Additionally, the presence of an interface manifests itself in a positional uncertainty in vector location. When the correlation window overlaps the interface, the centroid of the measurement area is moved from the center of the interrogation area towards one side. Attributing the vector to the geometrical centre of the interrogation window is therefore no longer suitable. Viscous effects moreover cause a difference in motion between flow and submerged object, leading to gradients in the velocity field close to the interface. In combination with improper vector location this is reported to bias the measurement (Keane and Adrian 1992).

In conclusion the following problems are identified as crucial for PIV measurements in wall proximity;

(a) signal truncation at the wall,
(b) presence of spurious light reflected from the wall,
(c) biased velocity estimates and
(d) insufficient wall-normal spatial resolution.

The remainder of the paper describes possible solutions to points (a) and (b) by means of image pre-processing and correlation schemes. Furthermore, point (c) is addressed recalling the vector-relocation technique. Finally the possible improvement of wall-normal resolution is handled by an adaptive algorithm based on non-isotropic resolution. The proposed methods are presented with computer simulated particle images and further assessed under experimental conditions.

3 Numerical assessment

Different pre- and processing methodologies will be assessed by means of Monte Carlo simulations with computer generated PIV images (Okamoto et al. 2000). The generated PIV images all had a maximum intensity level of 255 corresponding to a depth of 8bits. The background was simulated with a uniform component of 16% and a fluctuating term (i.e., pixel noise) of 3%. A seeding concentration of 0.08 particles per pixel^2 was applied where particles were distributed randomly in a Gaussian shaped laser sheet. Gaussian particle images were integrated over a pixel array with fill factor 0.7 representing the virtual sensor. A normal distribution was applied for the

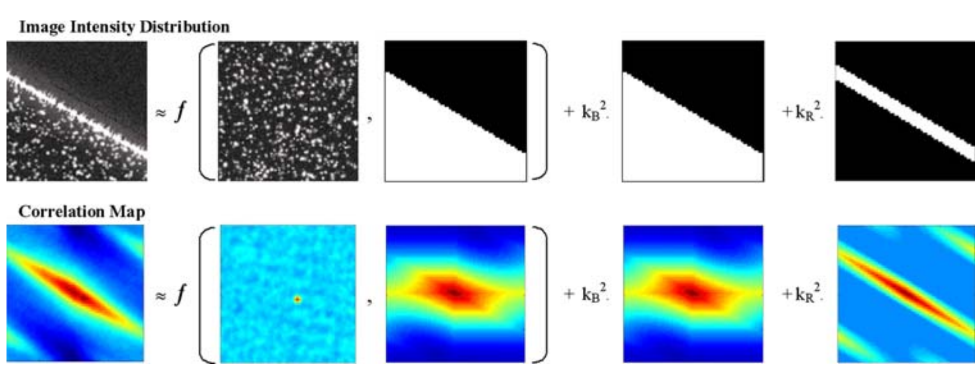

Fig. 2 (*Top*) The signal truncation can be represented as a multiplication between the undisturbed image and binary masks belonging to the intensity pedestal and reflections. (*Bottom*) Depicting only the dominant terms, the correlation of the images can be approximated as a summation of the cross-correlation of the undisturbed images and the individual autocorrelations

particle image diameters with a mean of 3 pixels and variance of 1 pixel. Two types of images were generated; the first image type contained a simple transition from the flow region to the object without interface. Reflections and flare were imposed in the second image type. For each of the image types the interface was placed either at 0° inclination or 30° to simulate respectively flat or inclined walls (Fig. 3). Tracer particles were uniformly displaced parallel to the interface by a finite amount. Interrogation windows were set to 33 pixels and did not overlap. For the two image types the case of 50% wall overlap ratio (WOR) between the correlation windows and interface was considered while preserving a high enough number of particle image pairs for reliable correlation.

3.1 Image pre-processing

In absence of temporal fluctuations in reflection and flare, background subtraction is in principle able to adequately remove the truncation and reflection terms '$k_B \cdot S$' and '$k_R \cdot T$' in the original image (Eq. 2). According to Wereley et al. (2002) the proper way is to select at each pixel location the minimum intensity over an ensemble of PIV image recordings. Having eliminated reflection and noise truncation (or in case of ideal intensity transition from flow to object, cf. image type 1), the intensity distribution involves only signal truncation. Comparison between correlation maps of the original and background subtracted image shows an almost complete removal of the reflection's and flare's autocorrelation (Fig. 4a vs. b). However, when coefficients 'k_B' and 'k_R' vary between images, background subtraction is unable to provide a valid noise estimate for each image individually, resulting in a distorted correlation map with only a minimal reduction in width of the reflection's autocorrelation (Fig. 4e vs. d).

Recalling the definition of the cross-correlation operation (Eq. 1), the remaining mean intensity pedestal will create an additional distortion. A direct approach is therefore to equalize the gray-scale values inside image areas

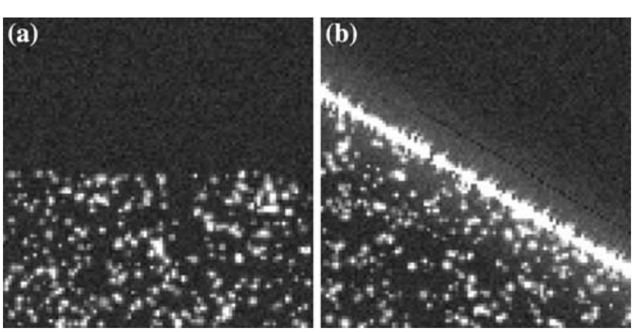

Fig. 3 Synthetic images: **a** Image type 1, 0° wall inclination. **b** Image type 2, 30° wall inclination

covering the flow and interface. Having identified the area within the correlation window containing flow-related information, its mean intensity is pasted within the masked area. Figure 4c indicates this operation to slightly enhance the peak detectability in case no reflection or flare is present. Otherwise, the improvement is more pronounced and the pasting operation furthermore reduces the DC component within the correlation map (Fig. 4f).

However, as image properties commonly have a spatial variation in the direction perpendicular to the interface, the mean intensity is not an accurate estimation for the amplitude of the pedestal. A pixel-wise approach will therefore be more accurate, such as e.g., the image subtraction proposed by Honkanen and Nobach (2005). Pedestals and reflections are removed from image pairs by subtracting each consecutive image within a pair i.e., $I_b - I_a$. The autocorrelation function of the signal truncation is no longer present and a distinct correlation peak is retrieved (Fig. 4g). Nevertheless the subtraction also removes objects with displacements smaller than one particle image width, which makes it unsuitable for boundary layers where the displacement gradually decreases towards zero when approaching the interface.

In conclusion, some attenuation of the effects of a stationary reflection can be achieved by means of local minimum intensity subtraction from each image. The problem of signal truncation can be partly addressed by masking techniques involving equalization of the mean intensity throughout the image. However, as image pre-processing does not allow a complete removal of the artifacts prior to the correlation operation, the correlation operator itself must be adapted in an attempt to reduce the prominence or effect of the autocorrelations related to the DC components.

3.2 Adapted correlation schemes

Since Willert and Gharib (1991) introduced the concept of digital image processing techniques in PIV, the use of fast Fourier transforms (FFT) for the image cross-correlation operation has become widespread. FFT is however sensitive to signal dependency both in the amplitude and phase domain. This is noticeable by the large peak at the origin of the correlation map originating from the image's DC component (Fig. 5a). In this case the particle displacement peak is hidden and cannot be recovered. For this reason Wernet (2005) proposes to filter the Fourier transform of each interrogation area such that only the phase contributes to the cross-correlation. After filtering, the correlation map shows two distinct Dirac-functions at the origin and most probable tracer displacement (Fig. 5b). However, when dealing with sub-optimal conditions (number of effective particle image pairs) we observed that the central peak can outgrow the true peak, decreasing detectability.

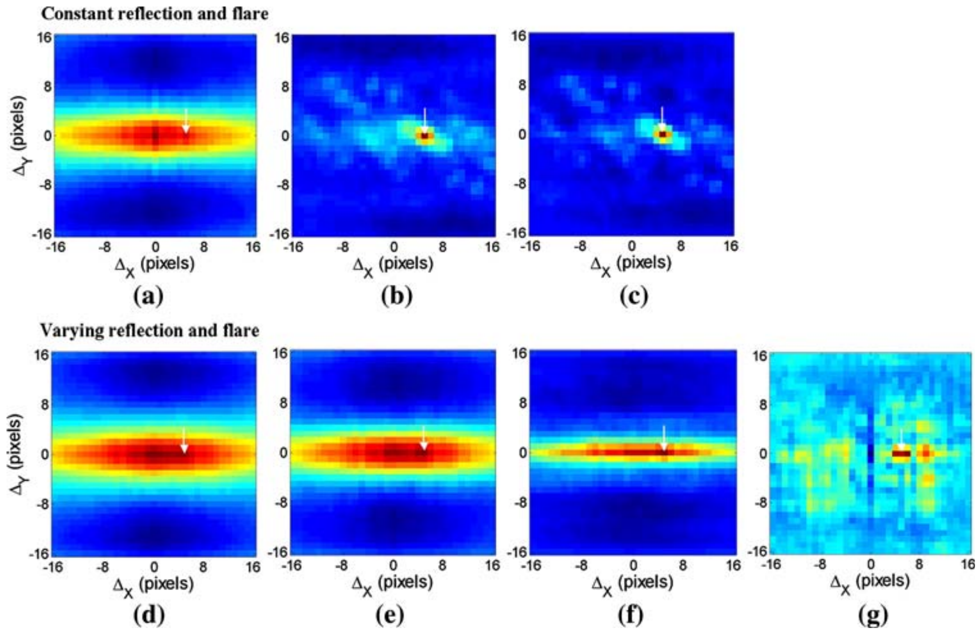

Fig. 4 Typical correlation maps for images of interfaces at 0° inclination with constant (*top*) and varying reflection and flare (*bottom*). Imposed displacement peaks are indicated by the *arrows*. **a–d** No pre-processing, **b–e** background subtraction according to Wereley et al. (2002), **c–f** background subtraction and intensity fill within masked area, **g** image subtraction according to Honkanen and Nobach (2005)

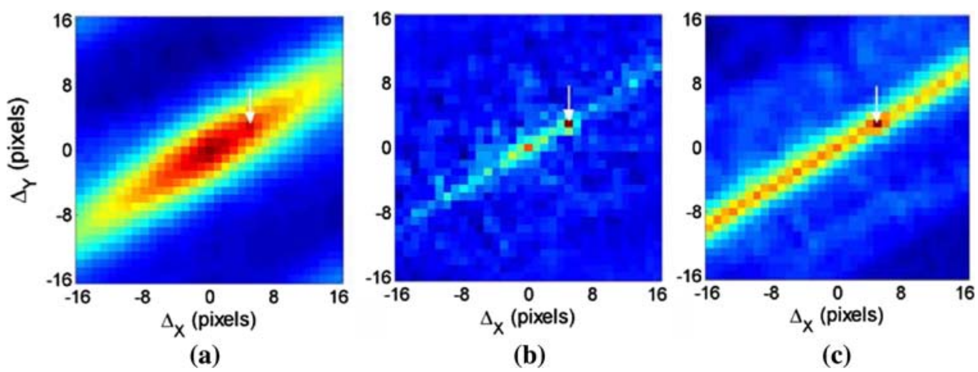

Fig. 5 Typical correlation maps for images as shown in Fig. 3b. The imposed displacement peak is indicated by the *white arrow*. Correlation using **a** FFT, **b** FFT with filtering (Wernet 2005), **c** symmetric mask exclusion direct cross-correlation

Results from Monte Carlo simulations with synthetic images of the second type for wall overlap ratios of 50% are presented in Table 1. Filtering the Fourier transform reduces the displacement error. Largest displacement errors are obtained with unfiltered FFT when correlation windows are not parallel to the interface i.e., 30° inclination. Though the filtered version shows to be an improvement in this case, the method is more susceptible to random errors due to a lack in tracer images causing frequently peak detection at the origin. The latter explains the higher RMS error for the filtered FFT method.

A simpler solution is to completely avoid signal truncation by excluding the interface region from the interrogation area. Ronneberger et al. (1998) applies direct cross-correlation (DCC) with an additional masking of the first interrogation window to exclude pixels covered by the interface from the correlation. DCC is beneficial in case of low seeding density as it utilizes an enlarged search area in which the smaller interrogation window is shifted. This explains its improved performances concerning displacement error and RMS error (Table 1). In addition, direct correlation does not assume periodicity in the image pattern as is the case with FFT. Here the authors propose to apply pixel exclusion in both interrogation windows and will refer to the method by the acronym symmetric mask exclusion direct cross-correlation (SME–DCC). The correct numerical implementation of SME–DCC is deemed

Table 1 Displacement error and RMS error after application of different correlation schemes to synthetic images of type 2, imposing uniform displacement of 5 pixels over flat walls at 0 and 30° inclination, correlation windows of 33 pixels, no mutual overlap and 50% WOR. Single correlation iteration

Correlation method	Displacement error		Displacement RMS	
	0° incl. (%)	30° incl. (%)	0° incl. (%)	30° incl. (%)
FFT no filtering	−80	<−100	32.8	6.8
FFT with filtering	−4	−27	14.6	48
SME–DCC	0	−0.2	2.8	0.6

important. Therefore the authors give more details in the appendix to the present paper. With DCC the prominence of the autocorrelation peak of the DC component has decreased compared to the original map (Fig. 5c). Moreover, the correlation peak has almost constant height, minimizing any bias towards the origin and reducing the possibility of false peak detection around the origin. At larger wall overlap ratios ($\geq$70%), the true peak is engulfed by the rim and can no longer be detected.

3.3 Vector relocation

Conventionally the obtained displacement vectors are attributed to the centre of the interrogation area. Tsuei and Savas (2000) discuss that when the centre of the correlation domain is located on a rigid stationary wall the obtained non-zero displacement vector is erroneous. The problem thus reduces to a proper repositioning of the vector representing the tracers' ensemble displacement when correlation windows overlap with the interface. Usera et al. (2004) propose to place the vector in the centre of the truncated correlation window as shown in Fig. 6.

In the present study the effect of vector relocation is assessed using synthetic data of a boundary layer with exponential velocity profile of equation;

$$u(y) = 3 \cdot \left(1 - e^{-\beta \cdot y}\right) \quad \text{where} \quad \beta = -\frac{\log(0.01)}{20} \tag{5}$$

The boundary layer thickness was set to 20 pixels. Correlation windows did not overlap mutually such as to study the effect of the velocity gradients for a single WOR between window and interface. The correlation operation was performed with SME-DCC. As reference, the response of a moving averaging filter (MA) on the imposed velocity distribution is plotted. The applied kernel size was 33 pixels excluding signal inside the interface in the averaging operation.

Without vector relocation the maximum overlap possible between correlation window and interface is 50%. At higher overlaps the geometrical centers of the windows fall inside the interface in which case the vectors are set to zero displacement to satisfy the no-slip condition. The latter causes a strong discontinuity in the velocity profile near the wall, which is more pronounced in the MA profile (Fig. 7a). More accurate displacement estimates are obtained by placing the vector in the geometrical centre of the information containing part of the correlation window. Relocation allows wall overlap ratios exceeding 50%, accompanied however by a higher displacement measurement uncertainty (Fig. 7b). Nevertheless, the obtained values better follow the imposed profile and the discontinuity near the wall has disappeared.

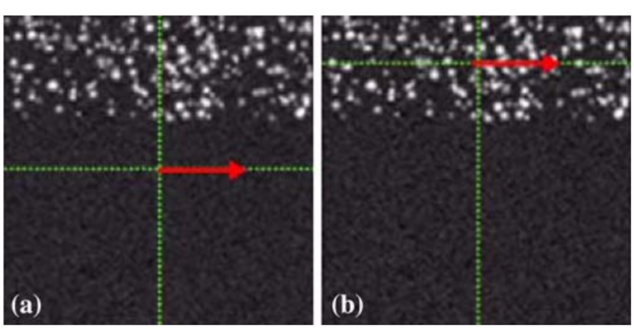

Fig. 6 Vector attribution **a** to the geometrical centre of the correlation window, **b** to the centroid of the seeded area within the correlation window

4 Adaptive interrogation near interfaces

Summarizing the previous results, the image pre-processing may enable to substantially attenuate the effect of reflections responsible for poor peak detectability. The latter is further enhanced exchanging the FFT method with SME–DCC. Finally the bias error can be compensated (if enough correlation signal is given) by a vector relocation technique. The problem however remains when reflections cannot be completely accounted for and when the interface is not aligned with the coordinates of the pixel grid. Moreover, as drawn in Fig. 7, even applying vector relocation, the spatial resolution close to the wall is in most cases the limiting factor for a PIV measurement.

In this section the earlier discussed schemes are implemented within an adaptive interrogation algorithm previously developed by the authors (Theunissen et al. 2007). The imposed adaptivity properly locates interrogation windows with the intention to sample regions with higher seeding densities and flow variances more densely with reduced window sizes. Briefly, the source density is mapped through a particle detection algorithm which allows dictation of the necessary window size by imposing a local image density. Estimates for the spatial fluctuations in the flow are taken as the spatial standard deviation of the velocity. Selected window sizes are inversely proportional to the seeding density and velocity standard deviation. Through a linear combination of velocity variance and source density the information concerning the signal distribution and flow scales is used in order to produce a single normalized distribution for the spatial sampling rate. A 2D transformation method distributes the window locations according to this sampling rate.

In the present case the aim is to keep constant the number of particle images when moving the interrogation area closer to the wall. This can be achieved by allowing the interrogation area to gradually expand in the direction tangent to the wall (assuming the flow to have a displacement parallel to the

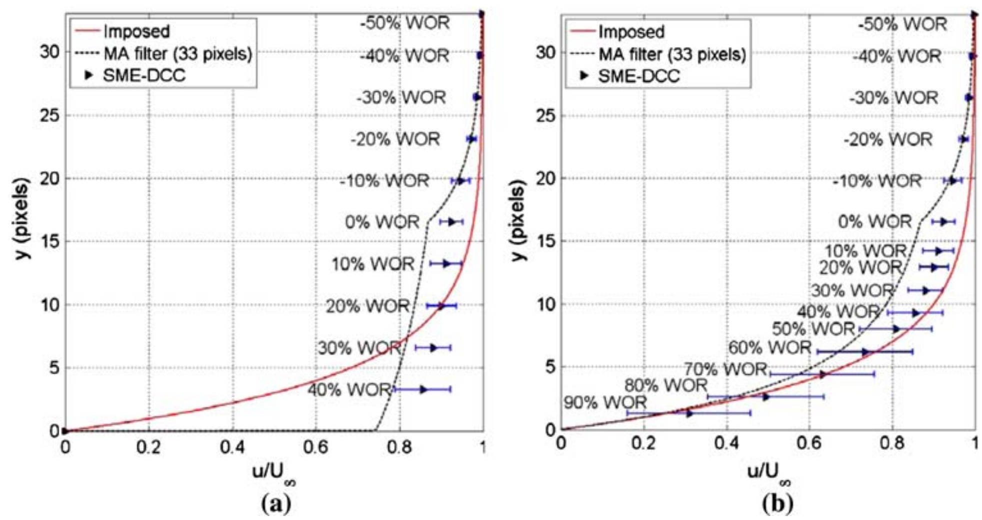

Fig. 7 Measured displacements for an imposed exponential velocity profile (*red line*) after a single iteration with a correlation window of 33 pixels applied to synthetic images of type 1 at different WOR with the interface at 0° inclination. **a** Vector positioned in the geometrical center of the interrogation window, **b** relocation of the vector to the centroid of the seeded area within the correlation window. *Horizontal bars* correspond to 95% confidence level

interface close to the object), resulting in a non-isotropic wall-normal resolution enhancement. The evolution of the window aspect ratio 'AR' with wall-normal distance '$d\xi$' is described by the following relation

$$\begin{aligned}\mathrm{AR}(\mathrm{d}\xi) &= \frac{W_{S\eta}(\mathrm{d}\xi)}{W_{S\xi}(\mathrm{d}\xi)} \\ &= \mathrm{SF}_{\max}\cdot\begin{cases}1 & \text{if } \mathrm{d}\xi < \beta \\ 1-\tanh\left(\pi\frac{\mathrm{d}\xi-\beta}{4\cdot\beta}\right) & \text{if } \mathrm{d}\xi \geq \beta\end{cases}\end{aligned} \tag{6}$$

where 'β' assumes a general value of 15 pixels, based on the typical lower size limit for a square interrogation window. Subscripts 'η' and 'ξ' refer to wall-tangent and normal abscissa of the coordinate system aligned with the interface (Fig. 9). Equation 6 incorporates a user-defined maximum stretching factor '$\mathrm{SF}_{\max}$', with representative values ranging between 2 and 6. Both rotation and stretching will increase the effective interrogation areas as cartooned in Fig. 8, which has a beneficial effect on the correlation robustness (Adrian 1991). Enforcing simultaneously a reduction in total correlation window size further limits any spatial modulation. Following the principles of adaptive interrogation, the sampling rate is modified approaching the wall, increasing the windows' mutual overlap such to minimize the error due to coarse spatial sampling (Theunissen et al. 2006).

The proposed methodology may be generalized for the case of curved interfaces by including the interface curvature radius 'ρ' as an additional parameter to control the window aspect ratio;

$$\begin{aligned}\mathrm{AR}(d\xi) = \mathrm{SF}_{\max}\cdot\left[1+(SF_{\max}-1)\cdot\min\left(1,\frac{W_S|_{\mathrm{d}\xi=0}}{|\rho|}\right)\right]^{-1}\cdot \\ \times\begin{cases}1 & \text{if } \mathrm{d}\xi<\beta \\ 1-\tanh\left(\pi\frac{d\xi-\beta}{4\cdot\beta}\right) & \text{if } \mathrm{d}\xi\geq\beta\end{cases}\end{aligned} \tag{7}$$

and

$$W_S = \sqrt{W_{Sx}\cdot W_{Sy}} = \sqrt{W_{S\eta}\cdot W_{S\xi}} \tag{8}$$

The local slope of the interface is obtained from a point-wise second order polynomial fit after successful identification of the interface border (Xu and Prince 1998; Scholz and Kähler 2004). With increasing flatness of the interface the curvature tends to zero, in which case a maximum stretching can be applied. The maximum length of the stretched window is then limited to '$W_{s\eta} \approx \mathrm{SF}_{\max}^{1/2}\cdot W_s$' with a corresponding minimum width of '$W_{s\xi} \approx W_s\mathrm{SF}_{\max}^{-1/2}$' where '$W_s$' symbolizes the side of a square window of equal area (Eq. 8). When the radius of curvature becomes significantly smaller compared to the correlation window, the aspect ratio must tend to unity (Fig. 8d). In this case the

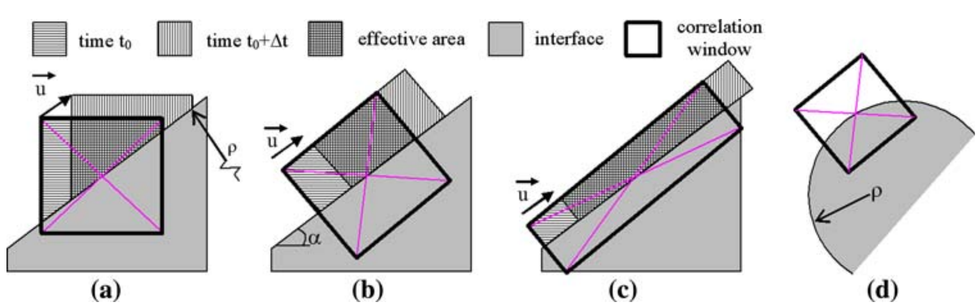

Fig. 8 Interface treatment: **a** standard, **b** rotation only, **c** rotation and stretching **d** effect of curvature

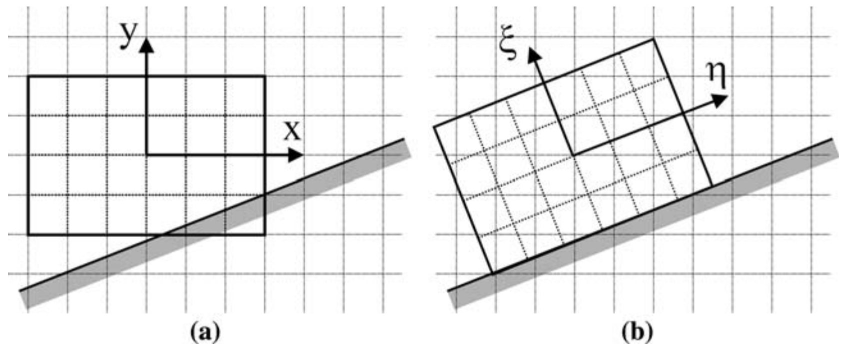

Fig. 9 Rotation of the correlation windows near interfaces requires re-interpolation of the original pixel intensities in the (x,y) coordinate system to the rotated (η,ξ) system

gradients in the spatial velocity distribution would anyway prohibit an accurate velocity measurement.

The calculation of the displacement within the rotated $(\eta,\ \xi)$-grid requires an image intensity re-interpolation (Fig. 9). A B-spline interpolation scheme (Unser et al. 1993) was implemented, constituting a trade-off between accuracy and computational effort. Rotation and iterative image deformation are combined in a single step, reducing both computation time and image degradation due to resampling (Scarano et al. 2005). Overall the additional processing time imposed by the adaptive interface interrogation is negligible compared to the computationally more intensive direct correlation approach. The latter causes increases in computational effort typically in the order of 20%, but is only needed however in a small fraction of the PIV image where an interface is present.

5 Experimental assessment

5.1 Subsonic turbulent boundary layer over a flat plate

The improved robustness and resolution of the proposed technique in case of real experimental conditions is attested in the following with the study of a subsonic turbulent boundary layer over a flat plate. Experiments on a turbulent boundary layer were conducted in a low speed wind tunnel with 40 × 40 cm^2 test section and Plexiglas side-walls minimizing reflections (Fig. 10a). The flow was seeded with particles of 1μm in diameter, produced by a fog generator. A Nd:Yag dual-head laser of 400 mJ provided the illumination and a 12 bit LaVision Imager Intense recorded the scattered light intensities. With a conversion factor of 1 pixel per 30 μm in the image plane, the field of view corresponded to approximately 4.2 × 3.2 cm^2. The boundary layer was measured at a free-stream velocity of 9.8 m/s. A tripping wire placed 2 m upstream ensured a fixed location of the transition to the turbulent regime with a Reynolds number of $Re_\theta = 1{,}900$ based on the momentum defect thickness 'θ'. Further details regarding the experimental setup can be found in Elsinga et al. (2007).

The tests are performed on the original images providing a reference for the more difficult case where the wall is inclined over 30° with respect to the CCD coordinates (Fig. 10b). The proposed correlation method is expected to be invariant of any rotation of the system of axis. To provide a comparison, the same sets of images were analyzed with a more conventional procedure (referred to in the following figures as "*conv.*") involving three iterative image deformation and refinement steps whereby correlation windows are placed on a Cartesian grid (Scarano and Riethmuller 2000). Windows mutually overlapped by 75% and were correlated with the conventional FFT procedure.

Overall 100 images were used in the statistical analysis. To limit the influence of pixel-noise, background subtraction was performed prior to the correlation procedure as proposed by Wereley et al. (2002). To assess the measurement capacities individually of the different image interrogation metrologies, no-slip boundary conditions were neglected during iterative image deformation.

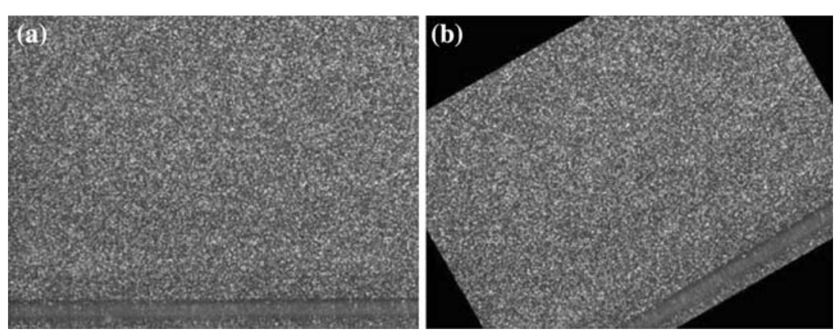

Fig. 10 Recordings of flat plate boundary layer experiment **a** original images, **b** images rotated over 30°

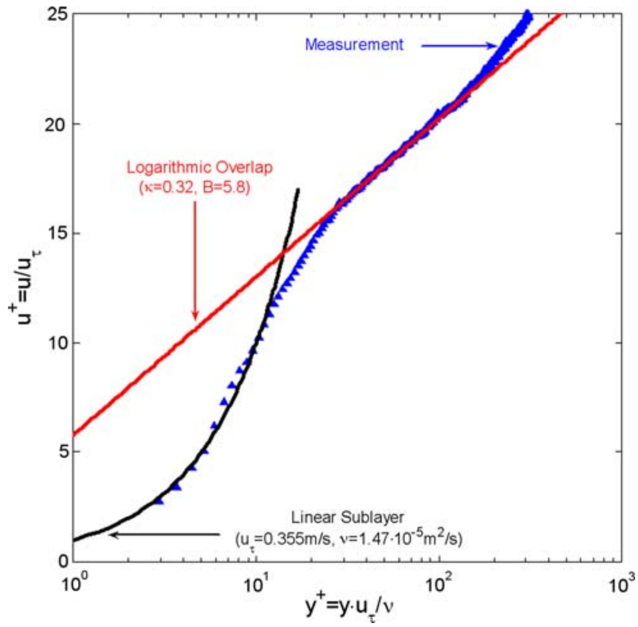

Fig. 11 Mean velocity profile obtained by ensemble correlation with superimposed law of the wall

Reference values for the wall-friction velocity were obtained by analyzing the original images by means of ensemble cross-correlation (Meinhart et al. 2000). Images were iteratively deformed while simultaneously reducing the interrogation area, producing a wall-normal spatial resolution of around two wall units (WU). The value for the wall-friction velocity '$u_\tau = 0.355$ m/s' was derived from a curve-fit of the inner-law to the resulting velocity profile (Fig. 11). Expressions for the inner variables and non-dimensional window size are given in Eq. 9 for conciseness.

$$u^+ = \frac{u}{u_\tau}, \quad y^+ = y\frac{u_\tau}{\nu}, \quad W_S^+ = W_S\frac{u_\tau}{\nu} \tag{9}$$

For the rotated images a typical distribution of 8000 correlation windows as applied by the improved adaptive interrogation methodology is depicted in Fig. 12a. Hereafter the adaptive algorithm combined with adaptive interface interrogation and correlation enhancements will be referred to in the graphs by the synopsis "*adaptive+a.i.i.+enh.*" From a visual inspection the sampling is denser in an area parallel to the interface. The latter is put further into evidence by plotting the probability density function (PDF) of the distance between the sample, i.e., center of the correlation window, and the wall (Fig. 12b). Combined with the algorithm's adaptivity of the sampling positions to the velocity fluctuations, a re-interpolation of the unstructured data to a Cartesian grid with approximately 1.5 WU (2 pixels) spacing was permitted.

Further rotation and stretching of the interrogation areas parallel to the inclined wall become prominent when zooming in on the interface (Fig. 12a). The evolution of the tangent and normal correlation window sizes '${W_{S\eta,\xi}}^+$' (expressed in wall units) with normal distance from the wall is presented in Fig. 13a. Within 11 WU windows remain constant in size with normal and tangent extensions of respectively, 6.4 and 40 wall units, corresponding to a maximum stretching factor of around 6. Beyond, the window aspect ratio gradually decreases tending towards a square-shaped interrogation area at 50 WU (Fig. 13b).

Averaged non-dimensional velocity profiles obtained by the extended adaptive and more conventional metrology are shown in Fig. 14a for the original boundary layer images. In the latter approach window sizes of 12.5 and 24.2 WU (respectively 17 and 33 pixels) were applied globally. With an overlap coefficient of 75% this translated in a data-spacing of respectively 3.1 and 6 WU, compared to 1.6 WU with the adaptive scheme. Due to the large window sizes with respect to the viscous length scale 'ν/u_τ' the conventional metrology is associated with insufficient resolution to measure the viscous sublayer (for which $y^+ \le 5$). The resolution of the wall-adaptive approach on the other hand is sufficient to resolve the viscous sublayer (Fig. 12b), yielding a u^+ y^+ profile fitting the theoretical models (Fig. 14a). Implementation of the enhancements discussed within this paper, being vector relocation and SME–DCC (hereinafter abbreviated to "*enh.*"), reforms the performances of the conventional interrogation approach in two ways. First, spatial resolution is increased through vector relocation, which is deducible in Fig. 14a

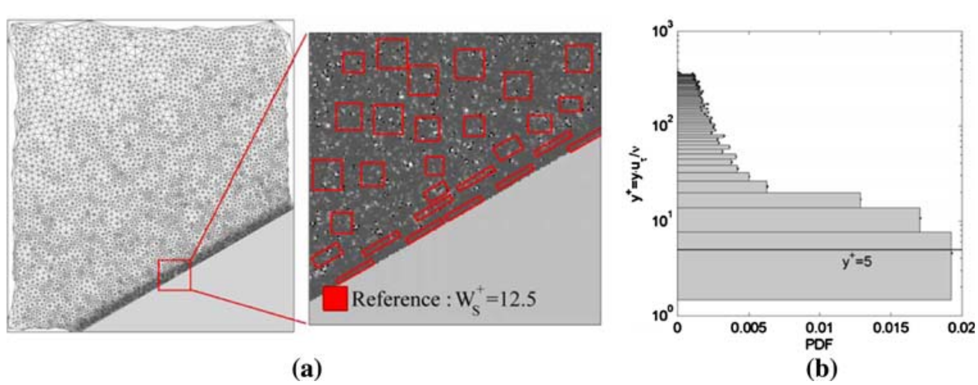

Fig. 12 Interrogation adaptivity **a** average window locations with zoom showing stretching and rotation of correlation windows, **b** probability density function of the distance between the interface and sample locations

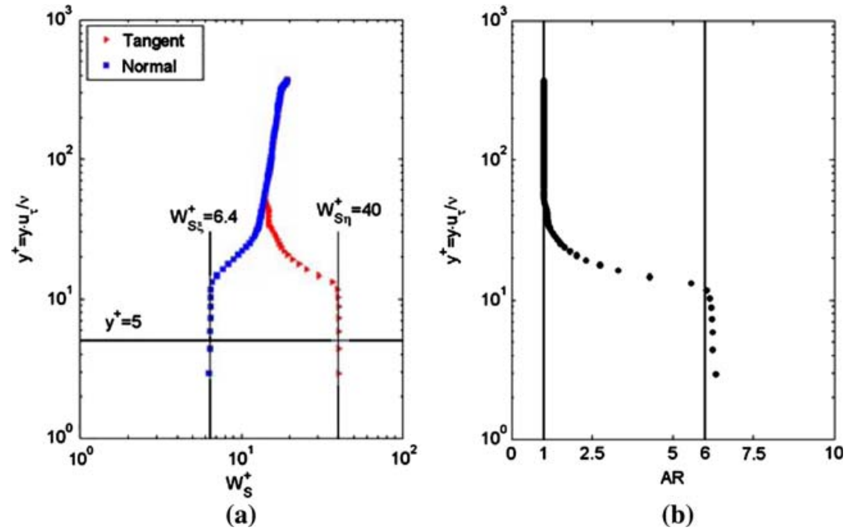

Fig. 13 Original boundary layer images: **a** evolution of the tangent and normal window sizes, expressed in wall units and **b** window aspect ratio as function of the wall-normal distance

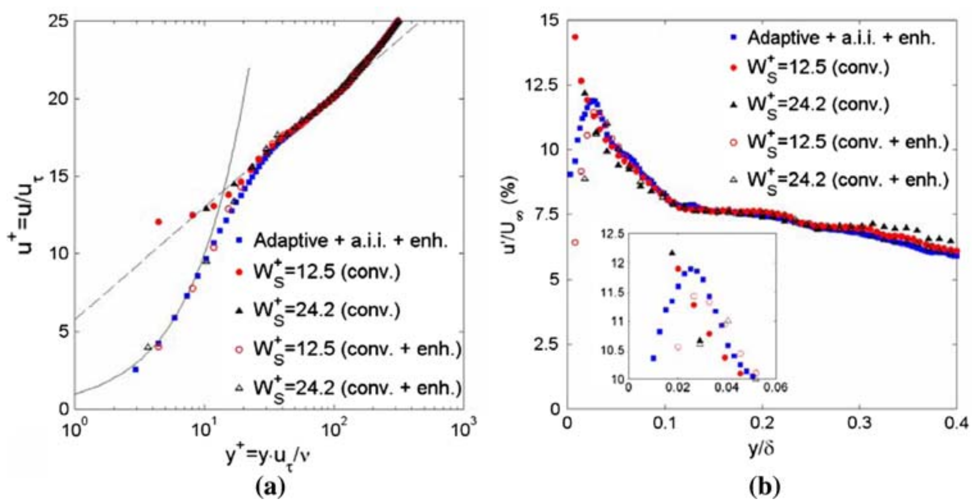

Fig. 14 Original boundary layer images: **a** mean velocity profile, **b** profile of fluctuation in the wall-tangent velocity component. Image interrogation was performed by the adaptive approach combined with adaptive interface interrogation (*a.i.i.*) and correlation enhancements (*enh.*) (*filled square*), the conventional approach (*conv.*) (*filled circle*, *filled triangle*) and the conventional approach including correlation enhancements (*conv. + enh.*) (*open circle*,*bullet*)

from the better fit of the non-dimensional profiles to both theory and results from adaptive interrogation. Second, the SME–DCC correlation scheme limits the number of erroneous vectors. The improved robustness is appreciable by plotting the RMS of the velocity component tangential to the wall (Fig. 14b). Whereas previously the RMS evolved inversely proportional to the wall distance 'y/δ'($\delta \approx 24$ mm), results now decrease near the wall and compare well with data reported by Klebanoff (1995). With decreasing window size the peak in RMS tends towards the adaptive measurement both in amplitude and spatial location, attesting the latter methodology to provide values representative of the investigated boundary layer.

Mean velocity profiles in inner-law scaling for the case of the rotated boundary layer images are presented in Fig. 15a. Results from the discussed image interrogation methodologies were re-interpolated to a pixel-wise grid beforehand allowing the extraction of the velocity data along a profile normal to the interface boundary. Conventional metrologies suffer from too poor resolution to resolve the linear sublayer (Fig. 15a), proving them not to be conducive for PIV analysis in proximity of interfaces not aligned with the coordinates of the pixel-grid. Amelioration of the spatial resolution is achieved by incorporating vector relocation and SME–DDC in exchange of FFT. Whereas before a maximum WOR of 27% could be encountered, the WOR now spatially varies, making the correlation windows more susceptible to a strong reduction in effective correlation area (Fig. 8a). In turn this increases the number of outliers and causes high RMS levels in the vicinity of the wall as shown in Fig. 15b. A compromise is therefore needed in parameter settings (i.e., window size) to find a trade-off between spatial resolution and robustness. Compared to the original case (Fig. 14a) the enhanced adaptive code on the other hand shows to return consistent results in mean velocity (Fig. 15a) while retaining robustness (Fig. 15b). Small dissimilarities between the velocity profiles are attributed first to uncertainties in wall-normal

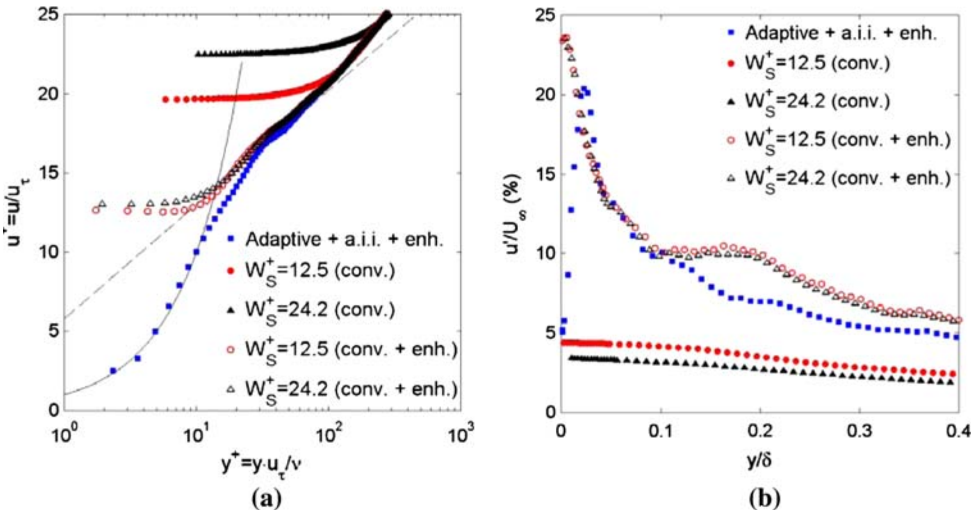

Fig. 15 Rotated boundary layer images: **a** mean velocity profile, **b** profile of fluctuation in the wall-tangent velocity component. Image interrogation was performed by the adaptive approach combined with adaptive interface interrogation (*a.i.i.*) and correlation enhancements (*enh.*) (*filled square*), the conventional approach (*conv.*) (*filled circle*, *filled triangle*) and the conventional approach including correlation enhancements (*conv. + enh.*) (*open circle*, *bullet*). Profiles are undersampled for readability by a factor **a** 2 and **b** 3 if $y/\delta < 0.04$ or 9 otherwise.

distance and second to poor image quality. The degradation in image signal is due to the performed morphological operation involving intensity re-interpolation. The latter further induces slightly enlarged window sizes away from the wall, modulating smaller fluctuations in the horizontal velocity component (Fig. 15b). Near the interface the loss in signal explains the deviation of the u^+y^+-profiles from the analytical function in the logarithmic overlap layer and the slightly higher amplitudes of the RMS distribution, while preserving the peak location.

5.2 Double compression ramp at Mach 7

To further attest the benefits of the correlation enhancements in wall-normal spatial resolution in vicinity of stationary interfaces, the case of a two-dimensional double ramp model with deflection angles of respectively 15° and 45°, placed inside a Mach 7 free stream (860 ± 10 m/s) is considered. A complete presentation of the experimental setup is described by Schrijer et al. (2006). Summarizing, experiments were conducted in a hypersonic facility based on the Ludwieg tube concept. Titanium dioxide seeding particles with a median diameter of 400 nm were introduced in the storage tube off-line by means of a high-pressure cyclone device. The procedure provided a relatively homogeneous seeding of the free-stream within a limited time interval (typically 20 ms) during the wind-tunnel run. A Quanta Ray Spectra-Physics dual head Nd:Yag laser served as illumination source. Scattered light was digitally recorded by a LaVision Imager Intense CCD cameras with 600 ns time separation between exposures. Approximately 32 pixels covered one millimeter giving a field of view (FOV) of 4.3 × 3.3 cm^2. The complex flow physics involved are visualized by the schlieren image presented in Fig. 16a where the analyzed field of view is indicated by the white rectangle. Leading edge shock, curved compression shock and the interaction region between the two are distinguishable.

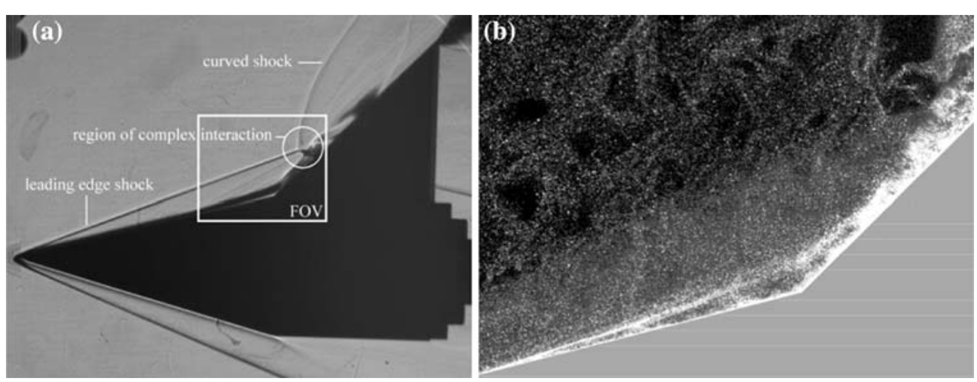

Fig. 16 **a** Schlieren image of the double wedge model at Mach 7. **b** Instantaneous PIV recording of the FOV (contrast has been enhanced for clarity)

Near the ramp corner the existence of boundary layer separation, reattachment and recirculation zones has been demonstrated extensively in both numerical and experimental studies (Korolev et al. 2002; Verma 2003; Fletcher et al. 2004, among others). However, detection of these phenomena with PIV measurements proves to be challenging. The strong spatial variations in seeding and flow velocity in the instantaneous PIV recording (Fig. 16b) cause the cross-correlation to fail either because not enough tracers are encountered within the interrogation area or because the flow velocity is too inhomogeneous within it. Larger correlation window sizes lead to an increase in correlation reliability and dynamic range but simultaneously lowers spatial resolution (Scarano and Riethmuller 1999). The latter explains why close to the wall, PIV measurements in general fail to sufficiently resolve the flow to infer small-scaled features. Besides the lack in tracer images due to large portions of the correlation windows overlapping the wall, strong reflections from the wall are encountered in the corner region. A strong bias of the measurements to zero is expected to appear in the proximity of the wall, which will further filter out smaller velocity fluctuations.

An example of a statistical mean of the total velocity is presented in Fig. 17, taking into account 40 background subtracted (Wereley et al. 2002) image snapshots. Here the PIV analysis was performed placing correlation windows of 0.43 mm^2 on a Cartesian grid with 0.19 mm spacing. The included iterative window deformation and refinement in the interrogation process cause velocity profiles to tend towards the imposed no-slip condition at the wall. None of the streamlines indicate however presence of a recirculation zone (Fig. 18a). Implementation of the SME-DCC routine and vector relocation is beneficial since the recirculation zone becomes discernible (Fig. 18b). Still, only through the adaptive approach can both the dynamical range and spatial resolution be optimized by, respectively, maximizing the window size range and relocation of the correlation windows (Theunissen et al. 2006). With the imposed adaptivity criteria the proximity of the ramp is oversampled (0.06 mm gridspacing) by correlation windows of 1.3 $\times$ 0.3 mm^2, which are aligned with the interface. The enhancement in wall-normal spatial resolution is appreciable as the thin layer of recirculating flow near the interface is now sufficiently resolved (Fig. 18c).

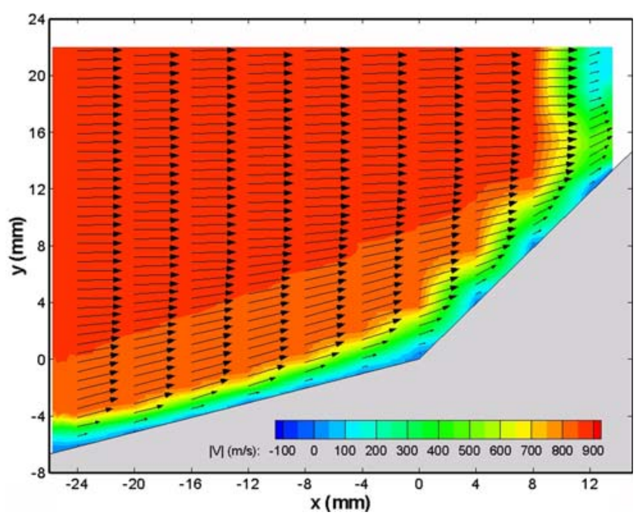

Fig. 17 Statistical mean of the total velocity for the FOV in Fig. 16a

6 Conclusions

In proximity of a wall, conventional correlation methodologies suffer from large distortions in the correlation map due to signal truncation and reflections. In this paper, several common image pre-processing, image processing and data post-processing routines are considered in the attenuation of the bias towards zero of the measured displacement and the probability of false peak detection. An assessment has been performed by means of Monte Carlo simulations with computer generated PIV images representative of fields of view involving static interfaces.

Local minimum intensity subtraction combined with equalization of the mean intensity throughout the image has been shown to be effective when reflections do not possess a temporal variation in intensity and image properties do not vary spatially. Under the opposed circumstances pixel-wise approaches are more appropriate in the removal of the artifacts from the images, but inherently degrade the signal of importance. Furthermore, the problem of signal truncation

Fig. 18 Streamlines in vicinity of the ramp after analysis with **a** the conventional approach, **b** the conventional approach including correlation enhancements, **c** the adaptive approach combined with adaptive interface interrogation and correlation enhancements

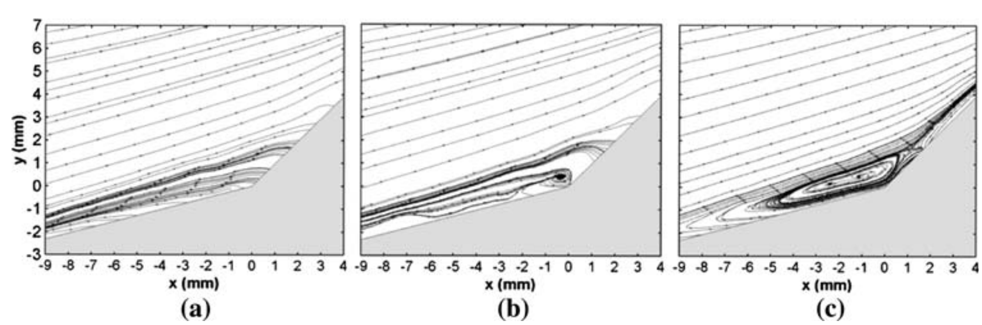

remains and demands proper windowing techniques for correlation. Given wall overlap coefficients below 70%, correlation of only the signal containing area within the correlation window by means of direct cross-correlation proved to be most effective when symmetrically excluding the masked regions. Further repositioning of the obtained displacement vectors towards the geometrical center of the information containing section reduces the positional uncertainty and increases the spatial resolution. The shortcomings of the conventional methodologies, as well as the effectiveness of the proposed enhancements, have been attested by application to experimental images of a flat-plate turbulent boundary layer. Ameliorations in spatial resolution and robustness of the image analysis were appreciable.

Despite all efforts, even after implementation of the correlation enhancements, windows are still susceptible to a low spatial resolution and a lack in number of effective particle image pairs when the interface is misaligned with the CCD coordinates. This reduction in effective correlation area causes a growing probability of erroneous displacement vectors. An innovative interrogation method has therefore been presented with the intention to increase robustness and resolution. Besides the implementation of vector relocation and DCC-based image correlation near the interface, the method incorporated wall adaptivity in an automated manner. The enhanced interface treatment consisted of (a) an increase in sampling rate in the vicinity of the wall, (b) rotation of the correlation windows parallel to the interface and (c) a reduction in wall-normal window size. Application of the proposed methodology to original and morphed flat plate boundary layer images has shown to yield consistent results both in velocity and turbulence intensity while retaining robustness. The benefits of the enhanced spatial resolution have been further demonstrated by comparing the PIV methodologies when applied to image recordings of a double compression ramp in a hypersonic flow. The adaptive approach was proven to possess sufficient spatial resolution to discern a recirculation zone near the corner, previously irresolvable by the conventional approach.

Acknowledgments The PIV images of the turbulent boundary layer and double ramp flow were kindly provided by Dirk Jan Kuik and Ferry Schrijer from TUDelft Aerospace Engineering. The presented work is supported by the Instituut voor de aanmoediging van innovatie door Wetenschap & Technologie in Vlaanderen (IWT, SBO project nr. 040092).

Appendix: Symmetric-mask-exclusion direct cross-correlation by means of FFT

Similar to the digital mask methodology proposed by Gui et al. (2003), the normalized correlation coefficient is defined as

$$\phi(m,n) = \frac{\sum_{i,j=1}^{k\cdot W_S} F(i,j)\cdot m_b(i+m,j+n)\cdot\left(I_{\mathrm{b}}(i+m,j+n)-\overline{I_{\mathrm{b}}}(m,n)\right)}{\sqrt{\sum_{i,j=1}^{k\cdot W_S} m_{\mathrm{b}}^2(i+m,j+n)\cdot\left(I_{\mathrm{b}}(i+m,j+n)-\overline{I_{\mathrm{b}}}(m,n)\right)^2}} \tag{10}$$

where

$$F(i,j) = \frac{m_{\mathrm{a}}(i,j)\cdot\left(I_{\mathrm{a}}(i,j)-\overline{I_a}\right)}{\sqrt{\sum_{i,j=1}^{k\cdot W_S} m_{\mathrm{a}}^2(i,j)\cdot\left(I_{\mathrm{a}}(i,j)-\overline{I_{\mathrm{a}}}\right)^2}} \tag{11}$$

To separate the seeded flow from the object area, binary masking arrays 'm_{a}' and 'm_{b}' are introduced for the first and second recording respectively (Fig. 19e,f). After expanding the multiplicative operation in the nominator

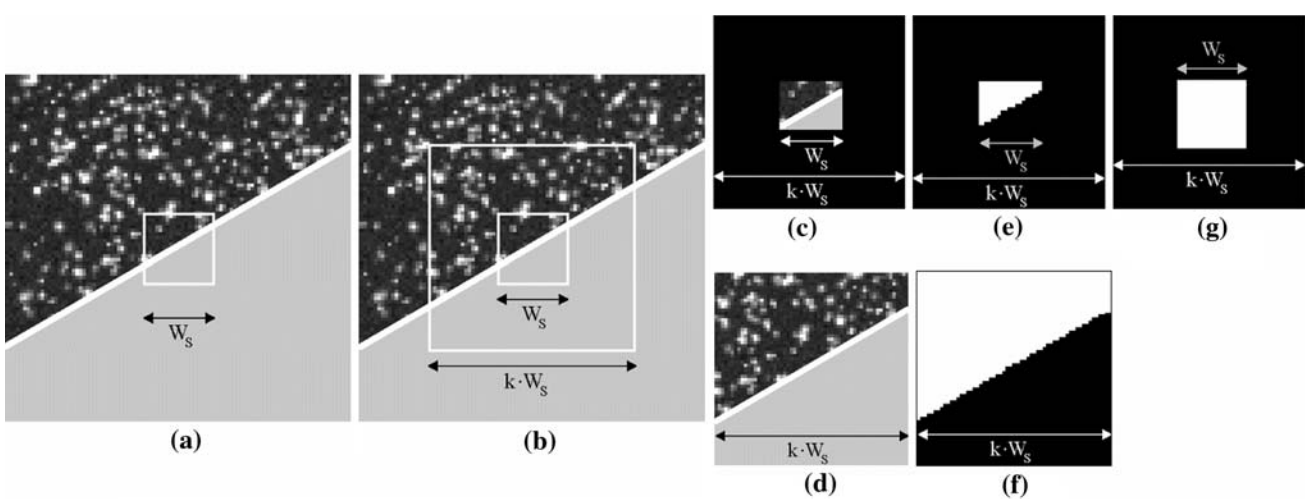

Fig. 19 **a** Image with selected interrogation area of size 'W_S', **b** second snapshot with extended search area '$k{\cdot}W_S$', **c** extended and padded interrogation area 'I_{a}', **d** selected search area 'I_{b}', **e** mask 'm_{a}' (*white* =1), **f** mask 'm_{b}', **g** mask 'W' used in calculation of mean intensity and covariance

of Eq. 10, each of the individual terms involves a cross-correlation, which can be performed by means of fast Fourier transforms. However, while 'F' needs to be computed only once before the correlation operation, both mean intensity '$\overline{I_b}$' and mask 'm_b' require recalculation for each offset (m,n). The latter necessitates a direct approach for the computation of 'ϕ', rendering the presented scheme computationally intensive.

Following the FFT-based free shape correlation (Ronneberger et al. 1998), the interrogation area in the first image is extended and padded with zeros to equal the size '$k \cdot W_S$' of the larger search area in the second partial image (Fig. 19a–d). This zero padding operation can be automatically taken into account by the binary mask 'm_a'. When measurement points are located on a structured grid factor 'k' is set to 2. With every iteration the disparity between the deformed images will converge to zero, eventually allowing values of 'k' approaching unity. In case of window rotation and non-isotropic sizing the dimensions of the enlarged search area are given by '$k_\eta \cdot W_{S\eta}$' and '$k_\xi \cdot W_{S\xi}$' respectively in wall-tangent and normal direction, where

$$k_{\eta,\xi} = 1 + \frac{\min\left(W_{S\eta}, W_{S\xi}\right)}{2 \cdot W_{S\eta,\xi}} \tag{12}$$

To negate the need of repetitive computation of '$\overline{I_b}(m,n)$' and '$m_b(m,n)$', the introduction of a third binary mask 'W' of similar size as the search area is proposed containing unity values inside the interrogation area and zero otherwise as depicted in Fig. 19g. Consequently, the mean operator can be translated into a correlation involving 'W', 'm_b' and 'I_b' (Eq. 13). Calculation of '$\overline{I_b}(m,n)$' in Eq. 13 is hence reduced to a one-time correlation operation by means of 2 Fourier transforms. Hereafter determination of '$\overline{I_b}$' at (m,n) becomes a mere lookup action.

$$\begin{aligned}\overline{I_b}(m,n) &= \frac{\sum_{i,j=1}^{k\cdot W_S} m_b(i+m,j+n)\cdot I_b(i+m,j+n)}{\sum_{i,j=1}^{k\cdot W_S} m_b(i+m,j+n)}\\ &= \left[\frac{W*(m_b I_b)}{W*m_b}\right]_{(m,n)}\end{aligned} \tag{13}$$

Concisely, the direct cross-correlation function can be expressed as a series of FFT operations (Eq. 14), which drastically reduces the computational effort compared to the direct spatial computation.

$$\phi = \frac{F*(m_b I_b) - \overline{I_b}(F*m_b)}{\sqrt{\left(W*m_b I_b^2\right) - \overline{I_b}^2(W*m_b)}} \quad \text{where } \overline{I_b} = \frac{W*m_b I_b}{W*m_b} \tag{14}$$

References

Adrian RJ (1991) Particle-imaging techniques for experimental fluid mechanics. Annu Rev Fluid Mech 23:261–304

Depardon S, Lasserre JJ, Boueilh JC, Brizzi LE, Borée J (2005) Skin friction pattern analysis using near-wall PIV. Exp Fluids 39:805–818

Elsinga GE, Kuik DJ, van Oudheusden BW, Scarano F (2007) Investigation of the three-dimensional coherent structures in a turbulent boundary layer. 45th AIAA Aerospace Sciences Meeting, Reno, AIAA-2007-1305

Fletcher AJP, Ruban AI, Walker JDA (2004) Instabilities in supersonic compression ramp flow. J Fluid Mech 517:309–330

Gui L, Wereley ST, Kim YH (2003) Advances and applications of the digital mask technique in particle image velocimetry experiments. Meas Sci Technol 14:1820–1828

Honkanen M, Nobach H (2005) Background extraction from double-frame PIV images. Exp Fluids 38:348–362

Keane RD, Adrian RJ (1990) Optimization of particle image velocimeters Part I double pulsed systems. Meas Sci Technol 1:1202–1215

Keane RD, Adrian RJ (1992) Theory of cross-correlation analysis of PIV images. Appl Sci Res 49:191–215

Klebanoff PS (1955) Characteristics of turbulence in a boundary layer with zero pressure gradient. Naca Report 1247

Korolev GL, Gajjar JSB, Ruban AI (2002) Once again on the supersonic flow separation near a corner. J Fluid Mech 463:173–199

Lin HJ, Perlin M (1998) Improved methods for thin, surface boundary layer investigations. Exp Fluids 25:431–444

Lindken R, Merzkirch W (2002) A novel PIV technique for measurements in multi-phase flows and its application to two-phase bubbly flows. Exp Fluids 33:814–825

Meinhart CD, Wereley ST, Santiago JG (2000) A PIV algorithm for estimating time-averaged velocity fields. J Fluids Eng 122:285–289

Okamoto K, Nishio S, Saga T, Kobayashi T (2000) Standard images for particle-image velocimetry. Meas Sci Technol 11:685–691

Ronneberger O, Raffel M, Kompenhans J (1998) Advanced evaluation algorithm for standard and dual plane particle image velocimetry. In: Proceedings of the 9th international symposium on applications of laser techniques to fluid mechanics, Lisbon, July 13–16

Scarano F, Riethmuller ML (1999) Iterative multigrid approach in PIV processing with discrete window offset. Exp Fluids 26:513–523

Scarano F, Riethmuller ML (2000) Advances in iterative multigrid PIV image processing. Exp Fluids Suppl S51-S60

Scarano F, David L, Bsibsi M, Calluaud D (2005) S-PIV comparative assessment: image dewarping+misalignment correction and pinhole+geometric back projection. Exp Fluids 39:257–266

Scholz U, Kähler CJ (2004) Automated image processing and segmentation for mask generation for PIV. In: Proceedings of the 12th international symposium on applications of laser techniques to fluid mechanics, Lisbon, July 12–15

Schrijer FFJ, Scarano F, van Oudheusden BW (2006) Application of PIV in a Mach 7 double-ramp flow. Exp Fluids 41:353–363

Shi J, Tomasi J (1994) Good features to track. In: IEEE Proc. Conf. on Comp. Vis. Patt. Recog., pp 593–600

Stanislas M, Okamoto K, Kähler C (2003) Main results of the first international PIV challenge. Meas Sci Technol 14:63–89

Theunissen R, Schrijer FFJ, Scarano F, Riethmuller ML (2006) Application of adaptive PIV interrogation in a hypersonic flow. In: Proceedings of the 13th international symposium on applications of laser techniques to fluid mechanics, Lisbon, June 26–29

Theunissen R, Scarano F, Riethmuller ML (2007) An adaptive sampling and windowing interrogation method in PIV. Meas Sci Technol 18:275–287

Tsuei L, Savas Ö (2000) Treatment of interfaces in particle image velocimetry. Exp Fluids 29:203–214

Unser M, Adroubi A, Eden M (1993) B-spline signal processing: Part II-efficient design and applications. IEEE Trans Signal Process 41(2):834–848

Usera G, Vernet A, Ferré JA (2004) Considerations and improvements of the analysing algorithms used for time resolved PIV of wall bounded flows. In: Proceedings of the 12th international symposium on applications of laser techniques to fluid mechanics, Lisbon, July 11–15

Verma SB (2003) Experimental study of flow unsteadiness in a Mach 9 compression ramp interaction using a laser schlieren system. Meas Sci Technol 14:989–997

Wereley ST, Gui L, Meinhart CD (2002) Advanced algorithms for microscale particle image velocimetry. AIAA 40(6):1047–1055

Wernet MP (2005) Symmetric phase only filtering: a new paradigm for DPIV data processing. Meas Sci Technol 16:601–618

Willert CE, Gharib M (1991) Digital particle image velocimetry. Exp Fluids 10:181–193

Xu C, Prince JL (1998) Snakes, shapes, and gradient vector flow. IEEE Trans Image Process 7(3):359–369